Fusion Engineering and Design 230 (2026) 115867

Contents lists available at ScienceDirect

Fusion Engineering and Design

journal homepage: www.elsevier.com/locate/fusengdes

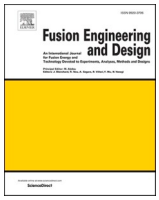

Mechanical characterization by tensile tests on miniaturised specimens extracted from an in-bore welded DN200 AISI316L pipe

Emanuele Fulco [a], Vincenzo Claps [a], Pasquale Guglielmi [a], Donato Sorgente [b,*], Rocco Mozzillo [a]

[a] CREATE, Engineering Department of Basilicata University, Campus Macchia Romana (PZ), 85100, Italy
[b] Department of Mechanics, Mathematics and Management, Politecnico di Bari, Viale Japigia 182, Bari, 70126, Italy

ARTICLE INFO

Keywords:
Demo
Remote maintenance
Pipe welding
In-vessel components
Breeding blanket

ABSTRACT

In the DEMO maintenance strategy, several pipes must be welded from the inside using in-bore systems, due to the limited space available. This constraint necessitates the development of bespoke solutions for both the welding process and the quality assessment of the welds. From the perspective of quality assurance, a key step is to verify whether the welded material meets the required mechanical performance. Given the different operational context compared to the ITER application, the development of a new remote handling strategy and a dedicated design for the in-bore tools is still in progress. Nonetheless, the qualification process has already begun to validate the selected welding process parameters.

In this work, the mechanical behaviour of the welded material is compared to that of the base material by extracting miniaturised specimens from the weld bead of a 16 mm-thick AISI 316 L pipe. The welding was carried out using multiple passes of a Tungsten Inert Gas (TIG) torch, and specimens were obtained via wire electro-discharge machining from three distinct locations within the weld: the top (close to the internal pipe diameter), the middle, and the bottom (near the external diameter). This sampling strategy allowed for the investigation of potential variations in mechanical properties arising from the different thermo-mechanical histories experienced across the weld thickness.

Tensile tests were performed on miniaturised specimens, and the results were analysed in terms of strength, ductility and fracture behaviour. These findings were compared with hardness measurements conducted on both the base material and the corresponding regions of the weld bead. Hardness profiles and 2D mapping revealed a through-thickness gradient with localised hard zones. The miniature tensile tests showed that all weld regions exhibited higher strength and lower ductility than the base material, while the tensile properties of the different regions of the fused zone were largely overlapping. Although a weak trend between hardness and yield strength can be recognised, hardness testing alone does not provide an exhaustive description of the mechanical behaviour of the fused and heat-affected material, confirming that miniature tensile tests remain essential for weld quality assessment in future qualification campaigns. These results provide a first mechanical basis for the qualification of in-bore TIG welds in DEMO-relevant service connections and support the future use of miniature tensile testing on limited-volume or activated material.

1. Introduction

As part of the European Research Roadmap to the Realisation of Fusion Energy [1], DEMO is conceived as the first device to demonstrate the feasibility of a fusion power plant, delivering net electrical power while operating in a quasi-stationary regime [2]. In such a context, plant availability becomes a key performance indicator: unplanned outages or extended maintenance periods not only reduce revenue but may even jeopardise the viability of the reactor if critical components cannot be repaired in situ. Maintenance is therefore a mission-critical function for DEMO [3].

The extreme radiation levels, high temperatures and restricted access within a fusion reactor impose that all in-vessel maintenance operations are performed remotely [4,5]. This requirement has driven the

* Corresponding author.
E-mail address: donato.sorgente@poliba.it (D. Sorgente).

https://doi.org/10.1016/j.fusengdes.2026.115867
Received 30 December 2025; Received in revised form 27 April 2026; Accepted 3 June 2026
Available online 8 June 2026

development of new maintenance concepts, tools and procedures that go beyond the capabilities of existing fission or conventional power plants. Among the various challenges, the management of service connections, including coolant, tritium, diagnostics and auxiliary systems, is particularly demanding. Plasma-facing, first-wall components are expected to be especially critical, due to the high number of pipe connections and the harsh operating environment in their vicinity [4,6].

To minimise downtime and reduce the risk of rendering the reactor inoperable, cutting and welding operations on these service lines must be highly reliable and fully automatable [7,8]. Moreover, the dense pipe routing envisaged in DEMO implies that joining tools must operate entirely in-bore, i.e. inside the pipe, since there is insufficient space for conventional external orbital systems [9,10]. Such in-bore cutting and welding equipment is not currently available off-the-shelf from industry, and therefore dedicated development activities are ongoing within the European DEMO programme. In particular, a Service Joining System (SJS) concept has been proposed, defining an overall joining strategy, an in-bore cutting and welding architecture and a roadmap for its maturation to an adequate Technology Readiness Level [3]. Proof-of-principle trials have already demonstrated the feasibility of the approach and identified the main technical risks that must be mitigated in view of DEMO application [11,12].

Within this framework, in-bore Tungsten Inert Gas (TIG) welding of large austenitic stainless steel pipes has been developed for DEMO-relevant blanket and first-wall circuits. Previous work has focused on the design of the in-bore welding head, on the optimisation of welding parameters for large-diameter, thick-wall pipes, and on the characterisation of the resulting welds in terms of defects and geometry [13]. However, a comprehensive assessment of the mechanical performance of these welds, particularly across the wall thickness and in configurations representative of future qualification campaigns or irradiated components, is still needed.

Miniaturised mechanical testing offers a promising route to address this need [14–16]. Small-scale tensile specimens can be extracted from limited volumes of material, including highly activated components, while still providing engineering-relevant information on strength and ductility when appropriately designed and tested. In the present work, miniaturised flat tensile specimens are machined from different through-thickness regions of a DN200, 16-mm-thick AISI 316 L pipe welded from the inside using a DEMO-relevant in-bore TIG procedure [13]. Tensile properties of the weld metal are determined and compared with those of the base material and correlated with hardness measurements along corresponding paths. The overarching objective is to evaluate the mechanical integrity of in-bore TIG welds for DEMO service connections and to demonstrate the suitability of miniature tensile testing as a tool for future weld-qualification.

The paper is organised as follows: Section 2 describes the welding procedure, the specimen extraction strategy and the experimental methods; Section 3 presents and discusses the hardness, tensile and post-mortem results; finally, Section 4 summarises the main conclusions and outlines future developments.

2. Material and methods

Tungsten Inert Gas (TIG, Gas Tungsten Arc Welding) welds were produced on AISI 316 L austenitic stainless steel pipes with an outer diameter of 212 mm, an inner diameter of 180 mm and a wall thickness of 16 mm, joined in a butt-joint configuration with J-shaped bevels (Fig. 1a) and 2 mm root faces to ensure self-alignment and a nominally zero gap between pipe ends.

An in-bore TIG torch, equipped with a 3.2 mm WLa10 tungsten electrode (30° tip angle) and a ceramic nozzle (19 mm diameter, 36 mm length), was used in combination with a hot-wire system feeding 0.8 mm AISI 316LSi filler wire at 65° to the electrode axis. The relative rotation between torch and vertically oriented pipe was obtained by mounting the lower pipe on a rotating table. Argon shielding gas was supplied both inside the pipe through the torch gas lens (25 L/min) and at the weld root on the outer surface (15 L/min) via an external backing-gas chamber. Multi-pass welding (root, hot, filling and capping passes) was carried out with pulsed current and controlled interpass

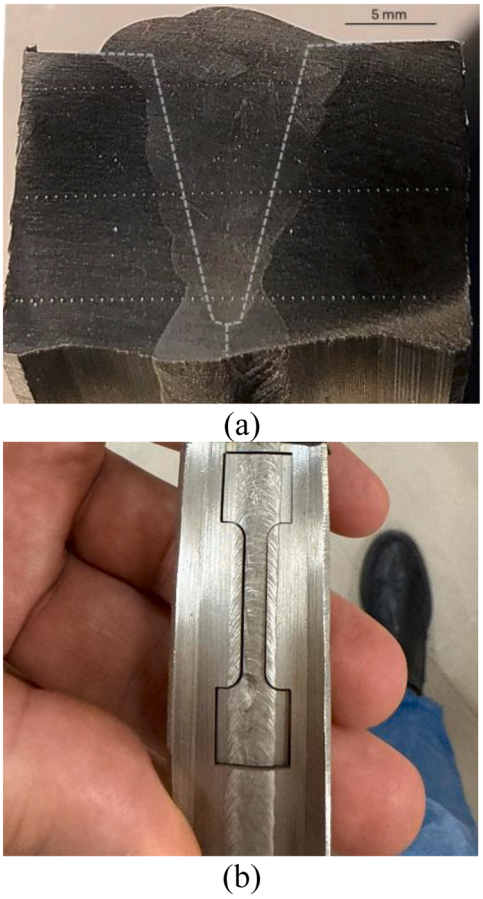

Fig. 1. (a) Cross section of the weld with dashed lines representing the bevel (before the welding) and the hardness measurements along the three paths. (b) Wire-electro-discharge machined ring portion of the welded pipe.

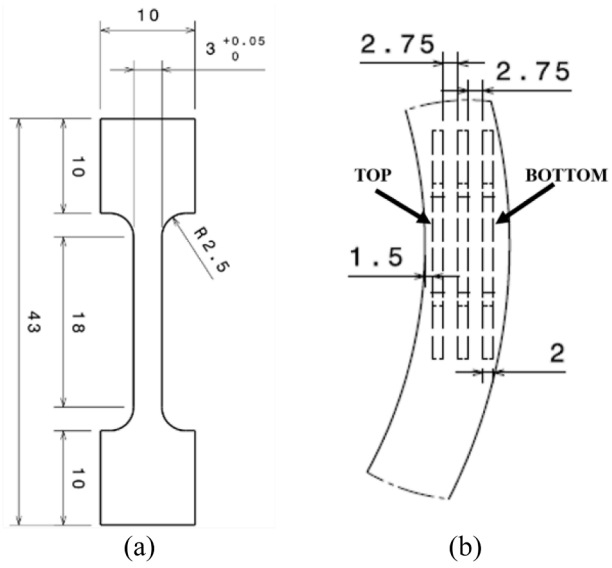

Fig. 2. (a) Miniaturised tensile specimen and (b) extraction scheme from the welded pipe (dimensions in mm).

temperature, allowing 10 min cooling between passes to keep the material below 150 °C, while temperature on the outer surface was monitored using K-type thermocouples. In particular, the temperature of 150 °C was selected to ensure both metallurgical integrity and dimensional stability, effectively preventing sensitization and preserving the alloy's corrosion resistance throughout the multi-pass process. Further details can be found in [13].

Miniaturised flat specimens (dimensions in mm as shown in Fig. 2a: parallel length 18 mm, gauge width 3 mm, fillet radius 2.5 mm, thickness 2.0 mm) were extracted from the welded pipes by wire electro-discharge machining. The parallel length was chosen as per the standard ISO-6892 with a coefficient of proportionality of 5.65 [17].

A ring segment approximately 25 mm wide was first removed from the welded pipe by band-saw cutting and then machined (Fig. 1b) to obtain specimens from three characteristic through-thickness positions: TOP, located close to the inner pipe surface on the weld cap side; BOTTOM, located close to the outer pipe surface on the weld root (root-pass) side; and MIDDLE, taken from the mid-wall thickness. Miniaturised specimens were adopted to enable mechanical characterization from limited material volumes and, therefore, arranged according to the extraction layout illustrated in Fig. 2b.

Six specimens were obtained from each characteristic region (TOP, MIDDLE, and BOTTOM), taken from different circumferential positions of the ring to ensure sampling reproducibility and representativeness across the weld.

Tensile tests were carried out at room temperature on a universal testing machine (Instron 5982, 100 kN capacity) under displacement control, with a constant crosshead speed of 1 mm/min. Axial strain was measured using a clip-on extensometer (model Instron 2620–601) attached to the gauge length. The specimens were not clamped directly in the machine wedges but were mounted in a dedicated gripping fixture, in which the specimen is housed and loaded through its shoulders (Fig. 3). After testing, it was verified that no significant plastic deformation occurred in the specimen heads. For each test, the engineering stress–strain curve was used to determine yield strength (YS), ultimate tensile strength (UTS) and uniform elongation (corresponding to the strain value at necking).

Prior to testing, the miniaturised specimens were laser-marked to create a reference grid for ductility measurement and for post-mortem observation of the strain distribution. For each specimen, the laser reference marks contained within the parallel length were selected, defining an effective initial gauge length of approximately 15 mm. After fracture, the two halves of the specimen were carefully reassembled by bringing the fracture surfaces back into contact, and the final distance between the same pair of reference marks was measured to calculate percentage elongation after fracture. The fracture surfaces were observed and acquired using a Nikon AZ100M optical microscope. Image acquisition was performed with the Extended Depth of Focus (EDF) function of the NIS-Elements software in order to obtain fully focused images of the fracture surface despite its three-dimensional topography. The resulting EDF images were then used to evaluate the extent of the fractured area by image-based measurement.

A Vickers hardness tester was used with a force of 1 kg_f (HV1) to measure the hardness across the weld along three paths corresponding to the TOP, MIDDLE and BOTTOM regions of the weld following the same procedure adopted in a previous work [13]. Additionally, a 2D hardness map covering the fused zone was produced on a different cross-section. Measurements were performed using a fully automated hardness tester equipped with a motorised cross table (Qness Q10), in accordance with the Vickers hardness standard (DIN EN ISO 6507), applying the load with a dwell time of 15 s.

In order to reveal the microstructure for optical examination, microstructural observations were carried out using a Nikon MA200 optical microscope after conventional metallographic preparation. The polished surfaces were electrolytically etched in a 40% aqueous NaOH solution using an applied voltage of 6 V for 20 s.

3. Results and discussion

3.1. Hardness measurement

In Fig. 4, the hardness profiles in the three different regions of the weld are reported.

Vickers hardness of the base material, measured on a section sufficiently far from the weld, is approximately 150 HV1. In contrast, all the values recorded on the cross section used in this work are significantly higher than this reference, indicating that the entire 25-mm-wide ring extracted from the welded pipe lies within the heat-affected zone (HAZ). This is consistent with the previous hardness survey reported in [13]. The hardness profiles along the TOP, MIDDLE and BOTTOM paths (Fig. 4) confirm the presence of a through-thickness gradient. The BOTTOM path, located near the outer surface of the pipe and corresponding to the weld root, exhibits the highest mean hardness and the largest scatter, with several local peaks clearly above the average value measured along the TOP path close to the inner surface. Nevertheless, hardness peaks can be observed also in the TOP path. The MIDDLE path shows an intermediate behaviour, with hardness levels and variability between those of TOP and BOTTOM.

The 2D hardness map in Fig. 5, superimposed on a mechanically

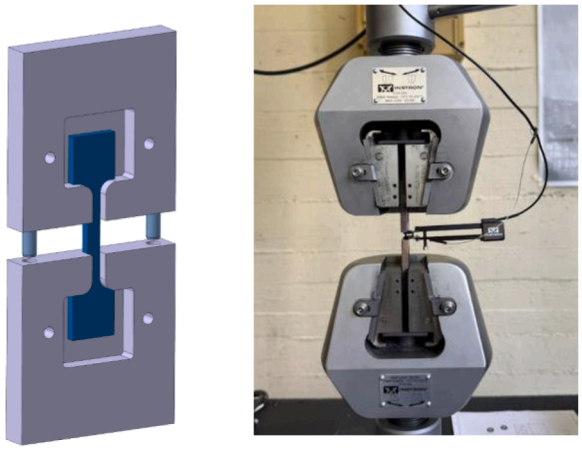

a b

Fig. 3. Fixture (a) for tensile tests on miniaturised specimens and test setup (b).

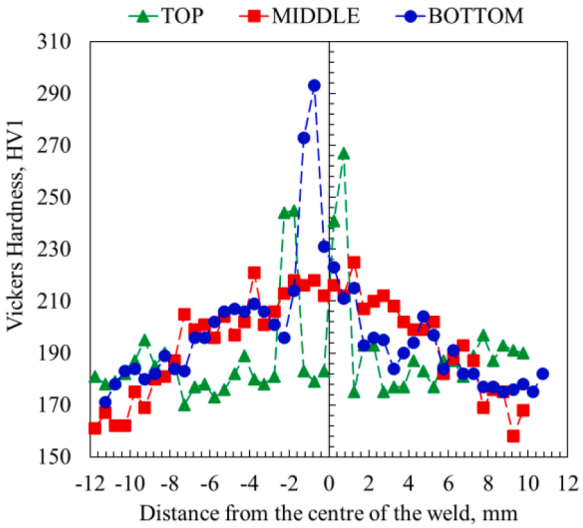

Fig. 4. Hardness values along the weld in the three paths.

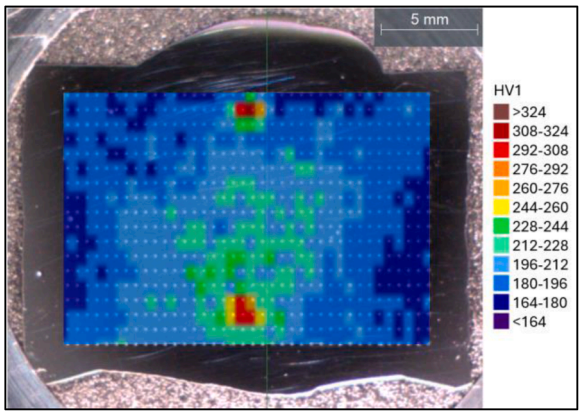

Fig. 5. Hardness map superimposed on a mechanically polished (but unetched) cross section of the weld.

polished (but unetched) cross section, provides a complementary picture of the spatial distribution of hardness. Harder regions are mainly concentrated in the lower part of the weld, close to the root, and extend towards mid-thickness, whereas the upper cap region appears predominantly in the blue–green range, closer to the base-material hardness level. The map also highlights that the hardest regions are not continuous layers but rather localised "islands" within an otherwise more homogeneous matrix.

Fig. 6 shows representative optical micrographs of the etched fusion-zone surface, acquired at the locations corresponding to the local hardness peaks (red arrows) identified in the hardness map reported in Fig. 5. The optical micrographs acquired in the TOP and BOTTOM regions display the classical resolidification morphology of multipass TIG AISI 316 L weld metal, i.e. a cellular/dendritic fusion-zone substructure, exhibiting a predominantly austenitic matrix containing a discontinuous network of residual δ-ferrite [18,19]. At the same time, despite the different average hardness measured in the TOP and BOTTOM regions, no obvious optical-microscopy evidence of a systematic microstructural difference between these two regions can be identified in the present observations. Rather, the local hardness peaks appear to coincide with positions where the Vickers indent falls across a local change in morphology, which suggests that the measured maxima may be associated with reheated/remelted interpass regions or adjacent solidification domains produced by pass overlap; analogous interface-related hardness variations have been reported in overlap regions of multi-run

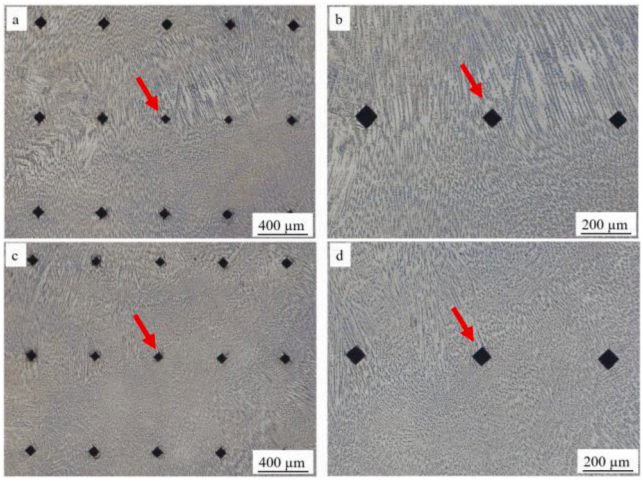

Fig. 6. Optical micrographs of local hardness-peak regions in the fusion zone: (a, b) TOP and (c, d) BOTTOM. (b) and (d) are higher-magnification views of (a) and (c), respectively.

welds and in layer-by-layer 316 L processing, where local interlayer hardness peaks were linked to differences in thermal history [20,21].

In this framework, the higher average hardness measured in the MIDDLE and BOTTOM regions may reasonably be related to the more severe cumulative thermo-mechanical history experienced by the material deposited during the earlier passes. In particular, the region close to the root is repeatedly reheated as subsequent passes are deposited, which can promote local microstructural modifications and contribute to hardening. At the same time, the progressive filling of the groove changes the geometrical constraint and the mechanical condition of the joint as welding proceeds, so that the material deposited in the lower and intermediate regions experiences not only a different thermal history, but also a different mechanical history, compared with the cap region. By contrast, the TOP region, associated with the final passes, is subjected to fewer subsequent thermal cycles and a different local constraint condition, which is consistent with its lower average hardness. This interpretation is also consistent with recent work on multilayer welding, showing that hardness variations in welded austenitic stainless steels can result from the balance between welding-strain hardening and recovery/recrystallization through changes in dislocation density, i.e. from the local thermo-mechanical history rather than from phase transformations alone [22].

3.2. *Tensile test results*

Fig. 7 report representative engineering stress–strain curves for the miniature specimens extracted from the TOP, MIDDLE and BOTTOM regions of the weld, together with the response of the base material.

For all three locations, the welded material exhibits higher stress levels than the base material over the whole strain range: at a given strain, the curves of the weld specimens lie systematically above the base-material curve. At the same time, fracture of the weld specimens occurs at lower strains, indicating a reduction in ductility with respect to the base material. The observed increase in strength as opposed to the reduction in ductility is consistent with the microstructural changes induced by welding which enhance deformation resistance while simultaneously restricting the material's capability for strain accommodation [23,24]. The scatter among weld curves is also larger than for the base material, particularly for specimens extracted from the BOTTOM region.

The distributions of YS and UTS are summarised in Fig. 8. All three weld regions (TOP, MIDDLE and BOTTOM) show YS and UTS values that are clearly shifted to higher levels compared with the base material. The three weld distributions are largely overlapping with each other, i.e. no strong monotonic trend is observed from TOP to BOTTOM, but the BOTTOM region displays the widest spread, with some specimens reaching the highest strength values of the whole dataset.

Fig. 9 shows the corresponding histograms of uniform elongation and percentage elongation after fracture. In this case the trend is opposite to that for strength: both uniform and total elongations of the weld specimens are generally lower than those of the base material, confirming the loss of ductility already apparent from the stress–strain curves. Again, the three weld regions exhibit broadly similar distributions, with a somewhat larger scatter in the BOTTOM data.

Overall, the welded material remains ductile, with all specimens displaying substantial plastic deformation prior to failure, but its deformation capacity is reduced compared with the base material.

Fig. 10 illustrates, for the base material, a miniature specimen in the as-machined condition and after tensile failure. The laser-marked grid appears as a regular array of circular spots on the undeformed specimen, whereas after testing the grid is visibly elongated along the loading direction, with a pronounced neck localised in the central portion of the parallel length. The marks on the specimen heads remain essentially undeformed, indicating that no significant strain develops outside the gauge and confirming the effectiveness of the dedicated gripping fixture, which loads the specimens through the shoulders rather than by direct

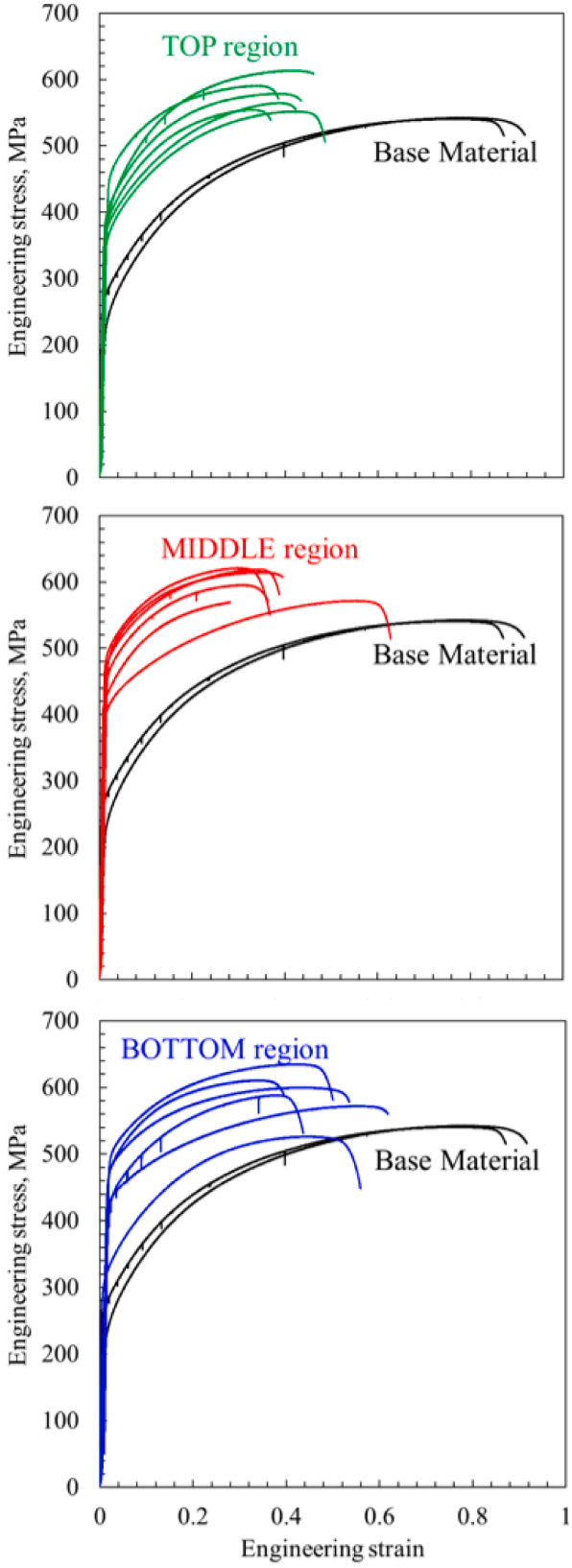

Fig. 7. Stress strain curve for the TOP, MIDDLE and BOTTOM regions of the fused zone of the weld and for the BM.

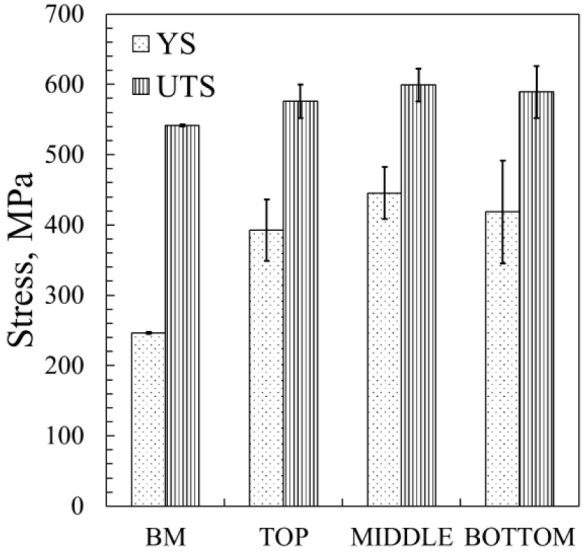

Fig. 8. YS and UTS for the BM and for the three different regions of the fused zone.

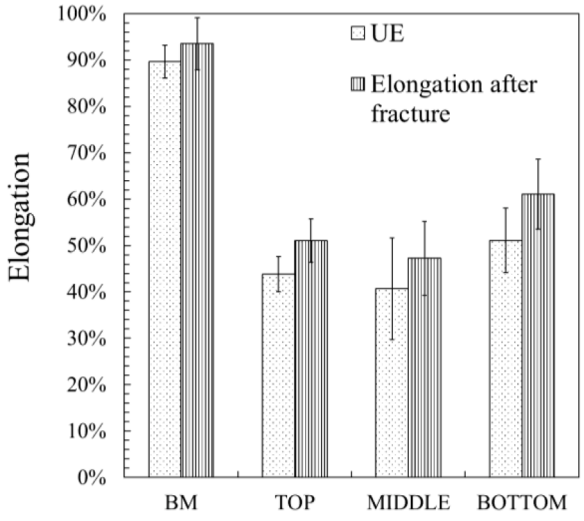

Fig. 9. UE (Uniform elongation) and Elongation after fracture.

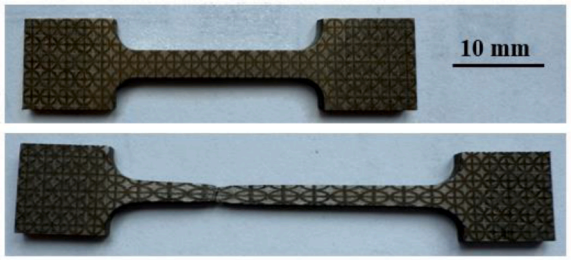

Fig. 10. Miniaturised specimen before and after the tensile test (BM).

clamping of the heads.

Fig. 11 compares the region around the neck for a specimen extracted from the base material and a specimen taken from the fused zone (MIDDLE). In the base material, the necked region is relatively broad and the distortion of the laser grid is gradual, indicating a more uniform distribution of plastic strain along the gauge. The specimen from the fused zone also exhibits a clearly developed neck and

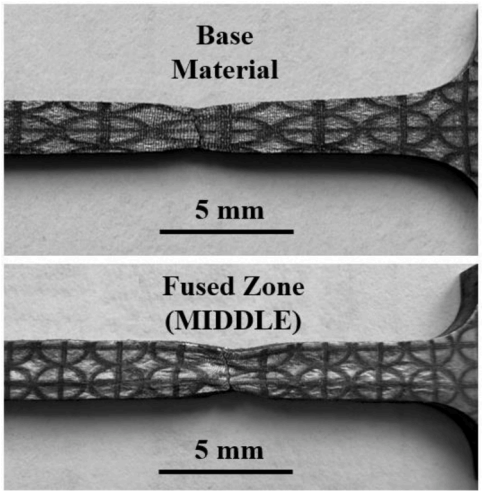

Fig. 11. Necked region of miniature specimens from BM and from fused zone (MIDDLE).

significant distortion of the grid, confirming that the welded material remains globally ductile, although the strain is more localised and the overall deformation capacity is lower than in the base material. In all cases, fracture occurred within the parallel length and not at the specimen shoulders, demonstrating that the testing setup did not introduce premature failure.

Fig. 12 compares the fracture sections of the BM (a) and of the fusion zone in the MIDDLE region (b). The BM shows a more uniform and regular plastic deformation, leading to a smaller final fracture area and therefore to a greater reduction of area. By contrast, the fusion zone retains a larger fracture section after failure, suggesting a less pronounced necking and a lower local ductility.

A possible explanation for the lack of statistically significant differences in YS and UTS, despite the marked local hardness variations measured between the TOP, MIDDLE and BOTTOM regions, is that the miniature tensile specimen still provides a more global mechanical response than the hardness test. In fact, although reduced in size, the tensile specimen gauge section (2×3 mm^2) samples a substantially larger material volume than a single Vickers indent, so that the measured tensile properties represent an average response of the heterogeneous fusion-zone material rather than the behaviour of individual local microstructural regions. Therefore, local hardness fluctuations associated with interpass reheating, remelting, or morphology changes may remain clearly detectable by microhardness mapping, while having a limited effect on the overall tensile response in terms of YS and UTS.

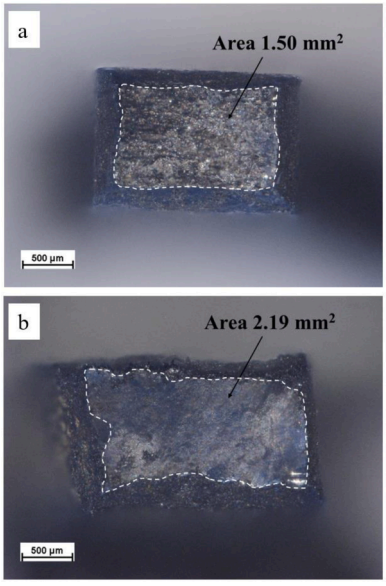

Fig. 12. Fracture sections after tensile testing: (a) base material and (b) fusion zone in the MIDDLE region. The dashed lines indicate the measured residual fracture area.

4. Concluding remarks and future work

The mechanical behaviour of an in-bore multi-pass TIG weld on a DN200, 16-mm-thick AISI 316 L pipe was assessed by hardness mapping and tensile tests on miniaturised specimens extracted at different through-thickness locations (TOP, MIDDLE, BOTTOM) and compared with the base material.

The main findings are:

- The Vickers hardness of the base material is about 150 HV1, whereas all measurements on the 25-mm-wide ring used for specimen extraction are higher, showing that the entire ring lies within fused and heat-affected material. Hardness is higher, on average, in the MIDDLE and BOTTOM regions, lower in the TOP region, and shows local peaks superimposed on this through-thickness trend, indicating a heterogeneous local thermo-mechanical history across the weld.
- The 2D hardness map reveals localised islands of high hardness rather than a continuous hardened layer. Optical micrographs acquired at selected hardness-peak locations show the classical resolidification morphology of multipass TIG AISI 316 L weld metal. No obvious systematic optical-microscopy difference was found between the TOP and BOTTOM regions, despite their different average hardness. The local hardness peaks appear instead to be associated with local changes in morphology, likely related to reheated/remelted interpass regions or adjacent solidification domains produced by pass overlap.
- Miniaturised tensile tests show that all weld regions have yield strength and ultimate tensile strength systematically higher than the base material, whereas uniform elongation and elongation after fracture are reduced. The three weld regions exhibit largely overlapping strength and ductility distributions, with no marked monotonic trend from TOP to BOTTOM, although BOTTOM shows the largest scatter and includes the highest strength and lowest elongation values. Post-mortem observations further show that all specimens fail in a ductile manner, with pronounced necking within the parallel length, while the welded material exhibits more localised deformation and a larger residual fracture section than the base material, consistent with its lower ductility.
- Despite the marked local hardness variations measured between the TOP, MIDDLE and BOTTOM regions, no statistically significant differences in YS and UTS were observed among the three weld locations. This indicates that the miniature tensile specimen still provides a more global mechanical response than the hardness test, so that local hardness fluctuations associated with interpass reheating, remelting or morphology changes remain clearly detectable by microhardness mapping, while having a limited effect on the overall tensile response.

The investigated welding procedure produces joints with strength exceeding that of the base material but reduced ductility, without evidence of a detrimental through-thickness gradient in tensile properties, and the combined hardness–miniature tensile approach proves effective for DEMO-relevant weld qualification.

Future work will complete the qualification of the in-bore TIG welding procedure by including standard transverse tensile tests, bending tests and impact tests, in order to provide a comprehensive assessment of the mechanical performance of DEMO-relevant pipes welded with in-bore technology.

In addition, a more in-depth microstructural characterisation of the weld metal and heat-affected material will be carried out by higher-resolution techniques, such as SEM-based observations, in order to better identify the local morphological changes associated with the hardness peaks and the interpass regions. Finally, numerical simulation of the welding process will be developed to investigate in greater detail the local thermo-mechanical history of the material during the successive passes and to support the interpretation of the measured hardness and tensile behaviour.

CRediT authorship contribution statement

Emanuele Fulco: Writing – review & editing, Writing – original draft, Visualization, Software, Methodology, Investigation, Formal analysis. **Vincenzo Claps:** Writing – review & editing, Software, Methodology, Investigation, Conceptualization. **Pasquale Guglielmi:** Writing – review & editing, Visualization, Software, Methodology, Investigation, Formal analysis, Data curation. **Donato Sorgente:** Writing – review & editing, Writing – original draft, Visualization, Validation, Supervision, Methodology, Investigation, Funding acquisition, Conceptualization. **Rocco Mozzillo:** Writing – review & editing, Supervision, Resources, Conceptualization.

Declaration of competing interest

The authors declare that they have no known competing financial interests or personal relationships that could have appeared to influence the work reported in this paper.

Acknowledgments

This work has been carried out within the framework of the EUROfusion Consortium, funded by the European Union via the Euratom Research and Training Programme (Grant Agreement No 101052200 — EUROfusion). Views and opinions expressed are however those of the author(s) only and do not necessarily reflect those of the European Union or the European Commission. Neither the European Union nor the European Commission can be held responsible for them.

Data availability

Data will be made available on request.

References

[1] T. Donné, W. Morris (eds.) European Research Roadmap to the Realisation of Fusion Energy. EUROfusion Programme Management Unit, ISBN 978-3-00-061152-0, November 2018. https://euro-fusion.org/eurofusion/roadmap/.
[2] INTERNATIONAL ATOMIC ENERGY AGENCY, Fusion Key Elements , Non-serial Publications , IAEA, Vienna (2024), https://doi.org/10.61092/iaea.rjb6-m9r0.
[3] T. Tremethick, S. Kirk, K. Keogh, A. O'Hare, E. Harford, B. Quirk, Service joining strategy for the EU DEMO, Fusion Eng. Des. 158 (2020) 111724, https://doi.org/10.1016/j.fusengdes.2020.111724.
[4] O. Crofts, A. Loving, D. Iglesias, M. Coleman, M. Siuko, M. Mittwollen, V. Queral, A. Vale, E. Villedieu, Overview of progress on the European DEMO remote maintenance strategy, Fusion Eng. Des. 109-111 (2016) 1392–1398, https://doi.org/10.1016/j.fusengdes.2015.12.013.
[5] O. Crofts, A. Loving, M. Torrance, S. Budden, B. Drumm, T. Tremethick, D. Chauvin, M. Siuko, W. Brace, V. Milushev, M. Mittwollen, T. Lehmann, F. Rauscher, G. Fischer, P. Pagani, Y. Wang, C. Baars, A. Vale, EU DEMO Remote maintenance System development during the pre-concept design phase, Fusion Eng. Des. 179 (2022) 113121, https://doi.org/10.1016/j.fusengdes.2022.113121.
[6] C. Bachmann, F. Arbeiter, L.V. Boccaccini, M. Coleman, G. Federici, U. Fischer, R. Kemp, F. Maviglia, G. Mazzone, P. Pereslavtsev, R. Roccella, N. Taylor, R. Villari, F. Villone, R. Wenninger, J.H. You, Issues and strategies for DEMO in-vessel component integration, Fusion Eng. Des. 112 (2016) 527–534, https://doi.org/10.1016/J.FUSENGDES.2016.05.040.
[7] R. Mozzillo, C. Bachmann, G. Janeschitz, V. Claps, O.C. Garrido, H. Pan, F. Li, D. Sorgente, Replacement strategy of the EU-DEMO and CFETR breeding blanket pipes, Fusion Eng. and Des. 202 (2024) 114311, https://doi.org/10.1016/j.fusengdes.2024.114311.
[8] Y. Ren, R. Skilton, A review of pipe cutting, welding, and NDE technologies for use in fusion devices, Fusion Eng. Des. 202 (2024) 114396, https://doi.org/10.1016/J.FUSENGDES.2024.114396.
[9] S. Kirk, K. Keogh, L. Naidu, T. Tremethick, In-bore robotic laser cutting and welding tools for nuclear fusion reactors, Lasers Eng. 46 (2020) 295–304.
[10] J. Rey, C. Köhly, P.C. Polixa, J. Reimann, In-bore tools for blanket replacement in the Demo Fusion Reactor, in: Proceedings of the First IAEA Technical Meeting on "First Generation of Fusion Power Plants—Design and Technology", Vienna, Austria, July 5–7, 2005.
[11] K. Keogh, S. Kirk, W. Suder, I. Farquhar, T. Tremethick, A. Loving, Laser cutting and welding tools for use in-bore on EU-DEMO service pipes, Fusion Eng. Des. 136 (2018) 461–466, https://doi.org/10.1016/j.fusengdes.2018.02.098.
[12] D. Sorgente, R. Salvato, C. Bachmann, C. Gliss, G. Janeschitz, H. Pan, X. Zhou, H. Wang, R. Mozzillo, Overview of in-bore pipe cutting and welding tools for the maintenance of CFETR and EU-DEMO, Fusion Eng. Des. 203 (2024) 114478, https://doi.org/10.1016/j.fusengdes.2024.114478.
[13] D. Sorgente, R. Salvato, V. Claps, C. Bachmann, G. Janeschitz, R. Mozzillo, Advancements of testing activities for development of in-bore welding tool for large feeding pipes of in-vessel components, Fusion Eng. Des. 220 (2025) 115367, https://doi.org/10.1016/J.FUSENGDES.2025.115367.
[14] R.L. Klueh, Miniature tensile test specimens for fusion reactor irradiation studies, Nucl. Eng. Des., Fusion 2 (1985) 407–416, https://doi.org/10.1016/0167-899X(85)90028-X.
[15] M.N. Gussev, R.H. Howard, K.A. Terrani, K.G. Field, Sub-size tensile specimen design for in-reactor irradiation and post-irradiation testing, Nucl. Eng. Des. 320 (2017) 298–308, https://doi.org/10.1016/J.NUCENGDES.2017.06.008.
[16] L. Li, J.W. Merickel, Y. Tang, R. Song, J.E. Rittenhouse, A. Vakanski, F. Xu, Dataset of tensile properties for sub-sized specimens of nuclear structural materials, Sci. Data 12 (2025), https://doi.org/10.1038/s41597-024-04329-2.
[17] ISO/TS 6892-5. Metallic materials — Tensile testing — Part 5: specification for testing miniaturised test pieces, 2025.
[18] H.T. Serindağ, G. Çam, Multi-pass butt welding of thick AISI 316L plates by gas tungsten arc welding: microstructural and mechanical characterization, Int. J. Press. Vessels Pip. 200 (2022) 104842, https://doi.org/10.1016/J.IJPVP.2022.104842.
[19] A.C. Hedhibi, K. Touileb, R. Djoudjou, A. Ouis, H. Alrobei, M.M.Z. Ahmed, Mechanical properties and microstructure of TIG and ATIG welded 316L austenitic stainless steel with multi-components flux optimization using mixing design method and particle swarm optimization (PSO), Materials 14 (14) (2021) 7139, https://doi.org/10.3390/MA14237139.
[20] C. Penot, J. Wharton, A. Addison, Y. Wang, Q. Lu, Interpass temperature effects on WAAM ER316L stainless steel corrosion using potentiostatic pulse tests, Npj. Mater. Degrad. 7 (1) (2023) 89, https://doi.org/10.1038/s41529-023-00408-8.
[21] C. Wang, T.G. Liu, P. Zhu, Y.H. Lu, T. Shoji, Study on microstructure and tensile properties of 316L stainless steel fabricated by CMT wire and arc additive manufacturing, Mater. Sci. Eng., A 796 (2020) 140006, https://doi.org/10.1016/J.MSEA.2020.140006.
[22] L. Yu, K. Nishimoto, H. Hirata, K. Saida, Hardness prediction of the heat-affected zone in multilayer welded SUS316 stainless steel based on dislocation density change behavior, Metall. Mater. Trans. A 55 (6) (2024) 1788–1803, https://doi.org/10.1007/S11661-024-07318-7.
[23] A. Sriba, J.B. Vogt, S.E. Amara, Microstructure, micro-hardness and impact toughness of welded austenitic stainless steel 316L, Trans. Indian Inst. Met. 71 (9) (2018) 2303–2314, https://doi.org/10.1007/S12666-018-1362-4.
[24] A. Rajesh Kannan, N.S. Shanmugam, Some studies on mechanical properties of AISI 316L austenitic stainless steel weldments by cold metal transfer process, Lect. Notes Multidiscip. Ind. Eng. Part F164 (2020) 359–371, https://doi.org/10.1007/978-981-32-9433-2_32.